photonics

MDPI

Article

A Transmission-Type High-Efficiency Chiral Filter with Three Discrete Wavelength Responses Based on Oracle Bone Structure Metasurfaces

Bo Cheng [1,†], Tiancheng Xian [2,†], Longfeng Lv [3], Yuxiao Zou [4,5], Guofeng Song [3], Kunpeng Zhai [6,*] and Hanxiao Shao [3,*]

1 Sichuan Provincial Engineering Research Center of Thermoelectric Materials and Devices, Chengdu Polytechnic, Chengdu 610041, China; chengbo9610@semi.ac.cn
2 The Distinguished Teacher Workshop of Yuan Lin, Chengdu Paotongshu Primary School, Chengdu 610031, China; xtc202230@163.com
3 Institute of Semiconductors, Chinese Academy of Sciences, Beijing 100083, China; lflv@semi.ac.cn (L.L.)
4 Kunming Institute of Physics, Kunming 650223, China; 13307110322@fudan.edu.cn
5 National Key Laboratory of Infrared Detection Technologies, Kunming Institute of Physics, Kunming 650221, China
6 National Key Laboratory of Semiconductor Laser, Institute of Intelligent Photonics, Nankai University, Tianjin 300071, China
* Correspondence: kpzhai@nankai.edu.cn (K.Z.); shaohanxiao@semi.ac.cn (H.S.)
† These authors contributed equally to this work.

Abstract

Conventional chiral metasurfaces are typically restricted to a single resonant wavelength, which limits their ability to satisfy the requirements of broadband detection and multi-channel polarization manipulation. To overcome this limitation, this study numerically proposes a chiral metasurface based on an oracle-bone-inspired geometry. By combining dislocation with rotational symmetry breaking, the proposed structure enables pronounced circular dichroism responses at three wavelengths in the long-wave infrared region, reaching 0.68@λ_1 = 10.43 μm, 0.79@λ_2 = 10.8 μm, and 0.6@λ_3 = 10.9 μm. This design overcomes the single-wavelength limitation of conventional chiral metasurfaces and establishes a new paradigm for multi-wavelength chiral light-field manipulation. This research not only broadens the design scope of chiral photonics, but also provides a promising technical path for the development of highly integrated infrared polarization devices and multi-wavelength chiral sensing systems.

Keywords: chiral metasurface; oracle geometry architecture; circular dichroism

Check for updates

Received: 16 March 2026
Revised: 11 May 2026
Accepted: 12 May 2026
Published: 15 May 2026

Copyright: © 2026 by the authors. Licensee MDPI, Basel, Switzerland. This article is an open access article distributed under the terms and conditions of the Creative Commons Attribution (CC BY) license.

1. Introduction

Circular polarization, as a fundamental vector property of light, plays a crucial role in optics, materials science, and the life sciences. Traditionally, selective control of circular polarization has relied mainly on natural chiral crystals or optical systems composed of waveplates [1] and polarizers [2]. These components manipulate the final polarization state by introducing different phase delays or absorption losses for left-circularly polarized light (LCP) and right-circularly polarized light (RCP), depending on the intrinsic chirality or birefringence of constituent materials. A key performance metric for such devices is circular dichroism (CD), defined as the difference in absorption or transmission between LCP and RCP. Devices based on these principles have been widely applied in circularly polarized

optical communication [3], stereoscopic display [4], molecular chirality detection [5], and spin photonics [6]. Even so, conventional bulk materials and discrete optical components remain fundamentally limited. Their optical responses are strongly constrained by material properties and operating wavelength, which leads to fixed working windows and narrow spectral coverage. Their bulky form also makes them difficult to integrate into modern optical systems, particularly chip-scale photonic platforms. These drawbacks have motivated the search for compact platforms that can manipulate circular polarization more flexibly at the subwavelength scale.

The emergence of chiral metasurfaces [7–9] has opened a promising route toward overcoming these limitations. Metasurfaces are planar optical devices composed of subwavelength artificial atoms arranged in a prescribed manner. By tailoring the geometry, dimensions, and spatial arrangement of individual meta-atoms, metasurfaces enable flexible control over the amplitude, phase, and polarization of light waves [10–15]. Chiral metasurfaces are structures whose unit cells lack mirror symmetry, or whose overall arrangement breaks spatial inversion symmetry, thereby producing different optical responses to LCP and RCP. Owing to this geometrically induced chirality, metasurfaces can generate strong CD effects within ultrathin platforms, while their optical performance can be engineered through structural design rather than being limited by the intrinsic properties of natural materials. Despite these advantages, most reported high-performance chiral metasurfaces still operate at only one design wavelength or within a narrow spectral band [16–18]. This single-wavelength characteristic severely limits their use in applications such as multi-channel polarization multiplexing [19], wide-spectrum chiral sensing [20], and systems that must work with multiple discrete light sources. Although the need for multi-wavelength or broadband chiral devices is growing, current design strategies remain unsatisfactory. One mainstream approach is to incorporate multiple resonant elements into a single-layer superstructure in order to excite several spectrally separated chiral modes [21–23]. However, this substantially enlarges the design space, increases the cost of full-wave simulation, and often makes device performance more sensitive to fabrication errors. Another strategy is to use multilayer stacked structures, with each layer optimized for a specific wavelength [24–27]. This can ease the design burden at the single-layer level, but it introduces strict alignment requirements, raises fabrication complexity and cost, and weakens the usual advantages of metasurfaces in compactness and ultrathin integration. Therefore, there remains a clear need for a simple and robust metasurface architecture capable of generating strong multi-wavelength chiral responses.

To address this issue, this paper proposes and numerically validates a novel chiral metasurface inspired by the geometric architecture of oracle bone inscriptions. The design is motivated by the distinctive symmetry-breaking characteristics of oracle bone patterns. By introducing two coordinated symmetry-breaking operations, namely dislocation and rotation, into a single unit cell, the proposed structure supports multiple spectrally separated chiral electromagnetic modes within a simple single-layer configuration. As a result, the proposed metasurface exhibits pronounced CD responses at three discrete wavelengths (λ_1, λ_2, λ_3) in the long-wave infrared band, with CD values reaching 0.68, 0.79, and 0.6 respectively. Compared with existing schemes that rely on complex patterns or multilayer stacking, the oracle-bone-inspired architecture presented here offers clearer physical intuition and simpler geometric features. More importantly, it demonstrates that strong multi-wavelength chiral responses can be achieved in a single-layer metasurface through coordinated symmetry breaking, thereby overcoming the single-wavelength limitation of conventional chiral metasurfaces. This work provides a new design paradigm and a practical technical basis for compact multi-wavelength polarization optical components,

and may facilitate future applications in spectral detection, biomolecular identification, and quantum information processing.

2. Materials and Methods

Figure 1a shows the spatial configuration of the oracle bone script character "zi" in traditional Chinese culture, whose outline resembles an abstract image of a moving child. In this character, the head (highlighted by the green dashed circle) and the trunk remain upright, whereas the arms (highlighted by the blue dashed circle) are stretched straight and form a certain angle with the trunk. The legs (highlighted by the purple dashed circle) are bent and also form a certain angle with the trunk. This asymmetric arrangement of the limbs gives the pattern an intrinsic chiral character, because it cannot be superimposed onto its mirror image by any in-plane rotation or translation. Figure 1b shows the three-dimensional structure of the chiral metasurface induced by the geometric architecture of oracle bone script. The structure consists of a MgF_2 substrate at the bottom and a silicon film with a special hole array at the top. The thickness of the silicon film is 1.72 μm, and the direction of the incident light is along the positive *z*-axis. Figure 1c is the top view of the unit cell of the metasurface, which presents the geometric details of the special holes. The optical refractive indices of silicon and MgF_2 are taken from reference [28,29]. The transmission rate of the long-wave chiral metasurface based on oracle bone script is obtained by COMSOL Multiphysics software (version 5.6) as the area integral of the Poynting vector at the transmission port, which represents the electromagnetic energy flux density. For clarity, Figure 1d presents the two-dimensional cross-sectional view of the optical model in the XZ plane, although the actual model is three-dimensional. Periodic boundary conditions (PBCs) are applied to both sides of the model, and perfect matching layers (PMLs) are added at the top and bottom. The distance between the PML and the silicon metasurface is two wavelengths, and the incident and transmission ports are located in the middle of the PML and the metasurface. The mesh size of silicon is 40 nm. The number of PMLs is 20.

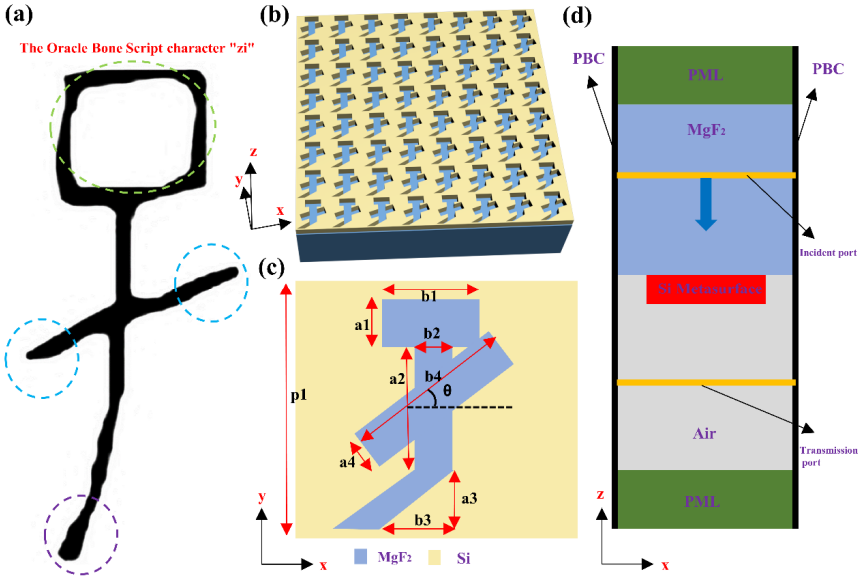


Figure 1. (**a**) The spatial configuration of character "zi" of the oracle bone script in traditional Chinese culture. (**b**) The three-dimensional structure of the chiral metasurface. (**c**) The top view of the oracle bone script metasurface. The parameters are p1 = 6.65 μm, a1 = 1.51 μm, a2 = 3.4 μm, a3 = 1.4 μm, a4 = 1.46 μm, b1 = 3.0 μm, b2 = 1.47 μm, b3 = 2.38 μm, b4 = 4.92 μm, θ = 30°. (**d**) A two-dimensional schematic diagram of the three-dimensional optical model. The real structure of the metasurface should correspond to the situation shown in Figure 1c.

3. Result

Figure 2 shows the transmission spectra and corresponding CD spectra of the designed oracle bone inscriptions metasurface in the 10.5 μm to 12 μm wavelength range. Under LCP incidence, the metasurface exhibits high transmission efficiency in the 10.4 μm to 10.8 μm band, with an average transmission rate exceeding 0.8, but there is a distinct transmission minimum at around 10.87 μm, marked as valley *a*. In contrast, under RCP excitation, the structure shows two significant transmission maxima at 10.71 μm and 10.86 μm, marked as peak *a* and peak *b*, respectively. Among these two resonances, peak *a* shows relatively strong transmission, approaching the LCP transmission at the same wavelength. The red dotted line in the figure represents the corresponding CD spectrum, defined as the difference between the transmission rates of LCP and RCP. As indicated by the light orange region, the spectral range with a CD value greater than 0.4 is defined as the effective chiral operating band of the metasurface. Within the intervals of 10.4–10.62 μm and 10.75–11.02 μm, the CD remains above this threshold, indicating efficient circular-polarization selectivity in these wavelength ranges. A closer inspection further suggests that if the non-target resonances (i.e., valley *a*, peak *a*, and peak *b*) could be suppressed and the transmission trend followed the extrapolated envelope shown by the black dashed line, the metasurface might exhibit a continuous high-CD response over the broader 10.4–11.2 μm range, thereby approaching broadband chiral operation.

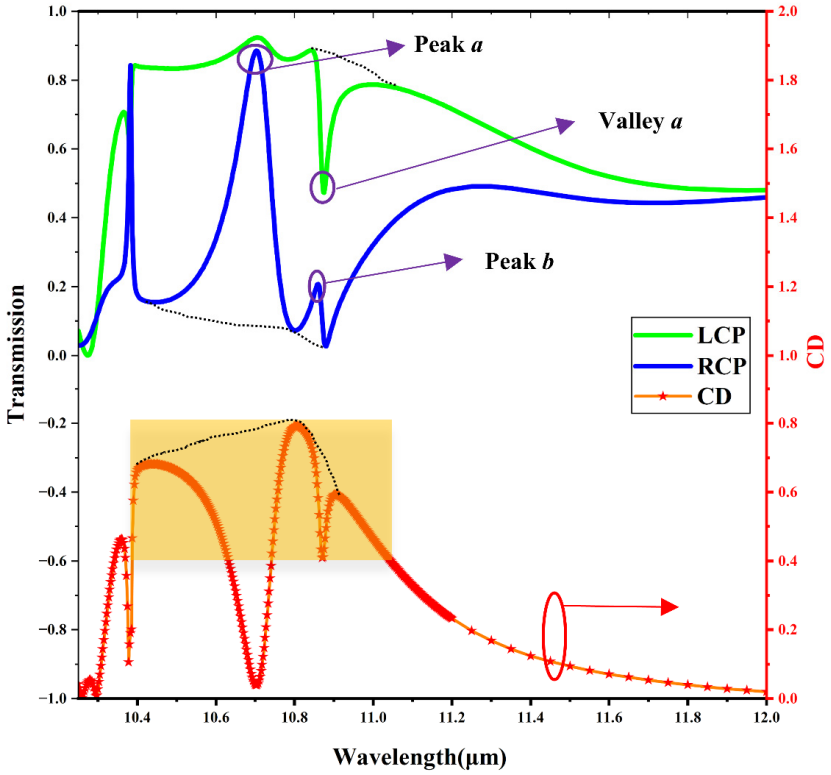


Figure 2. Transmission spectrum and CD spectrum of the oracle bone inscriptions metasurface. The black dashed line is the envelope line in the absence of corresponding peaks or valleys. The orange rectangle corresponds to the effective bandwidth of CD.

3.1. Chiral Evolution of Oracle Bone Script Metasurfaces

Chiral metasurfaces achieve selective responses to circularly polarized light through symmetry breaking in the subwavelength unit cell or in the overall arrangement of the microstructure array. In other words, their structures cannot be superimposed onto their mirror images through translation or rotation. Figure 3a–c illustrate the symmetry-breaking process of the proposed oracle bone inscriptions metasurface. The initial structure is a

rectangular cross unit (Figure 3a), corresponding to the image of a "child" with arms outstretched and legs upright. In Figure 3b, the first breaking of the spatial symmetry of the structure is achieved by introducing a lateral misalignment (Δx) in the legs. A further rotation by an angle θ then transforms the structure into a more asymmetric configuration, in which one arm is raised and the other is lowered, as shown in Figure 3c. As the dislocation and rotation are gradually introduced, the chiral characteristics of the structure become significantly stronger. Figure 3d,e quantitatively analyze the influence of these two symmetry-breaking operations on the CD performance. The number of discrete wavelengths with CD values exceeding 0.4 within the range of 10.4–11.2 μm range is counted after dividing this spectral interval into 80 equal parts. The CD threshold of 0.4 is chosen to maintain internal consistency and is not intended as a universal performance metric. Figure 3d shows that as the lateral misalignment Δx increases from 0 μm to 2.4 μm, the number of effective wavelengths undergoes a jump at Δx = 2.4 μm, increasing significantly from less than 5 to 20. Figure 3e shows that the rotation operation provides even stronger tuning capability, with Δx fixed at 2.4 μm throughout this process. When the rotation angle θ increases from 0° to 8°, the number of effective wavelengths doubles, and when θ reaches 32°, the number reaches its maximum of 58. These results clearly demonstrate that the combined dislocation–rotation symmetry-breaking strategy, enabled by the rich geometric degrees of freedom of the oracle-bone structure, provides an efficient way to tailor multi-wavelength chiral responses.

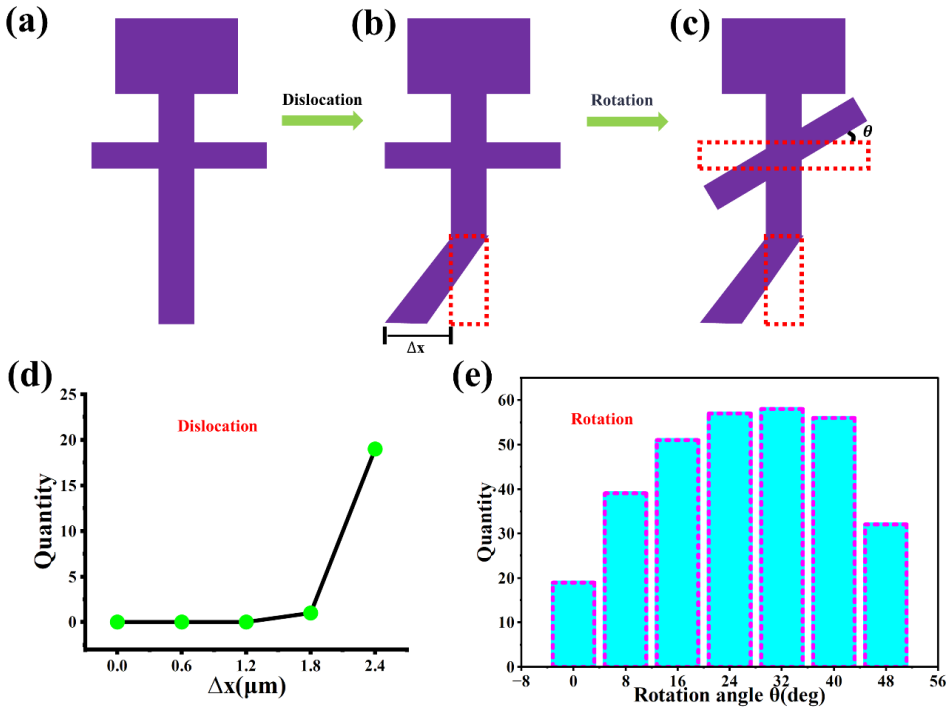


Figure 3. (**a**) The original C_2 symmetric structure. (**b**) The dislocation operation. (**c**) The combined effect of dislocation and rotation operations. (**d**) The number of wavelengths where CD exceeds the discrimination condition of 0.4 at different dislocation distances. (**e**) The number of wavelengths where CD exceeds 0.4 at different rotation angles.

3.2. Mode Analysis of Resonance Peaks

The multipole expansion method [30,31] is an analytical approach that decomposes the electromagnetic scattering response of complex nanostructures into a series of fundamental modes, such as electric dipole (ED), magnetic dipole (MD), electric quadrupole (EQ), magnetic quadrupole (MQ), and higher-order multipoles. Figure 4a shows the normalized multipole expansion spectrum of the oracle bone inscriptions metasurface. When the inci-

dent light is at the wavelength corresponding to peak *a*, the metasurface can be regarded as the result of the interference of a large number of EQs and a small number of MDs, leading to a maximum transmission phenomenon. When the incident light is at the wavelength corresponding to peak *b*, the transmission characteristics of the metasurface are mainly regulated by the cooperative effect of EQ, MD, and MQ, with their strengths decreasing in that order. The coexistence of these modes reflects the geometric complexity of the oracle-bone-inspired structure. Figure 4b–g show the magnetic-field-intensity distributions of the oracle metasurface in different XY cross-sections at the wavelengths corresponding to peaks a and b. The field is mainly confined within the silicon regions between adjacent unit cells along the horizontal direction. This suggests that the air–silicon–air configuration forms a typical three-layer dielectric waveguide, in which light is confined by reflection inside the high-refractive-index material and eventually forms a standing-wave pattern (indicated by the red regions). The strong field localization is consistent with the RCP transmission peaks.

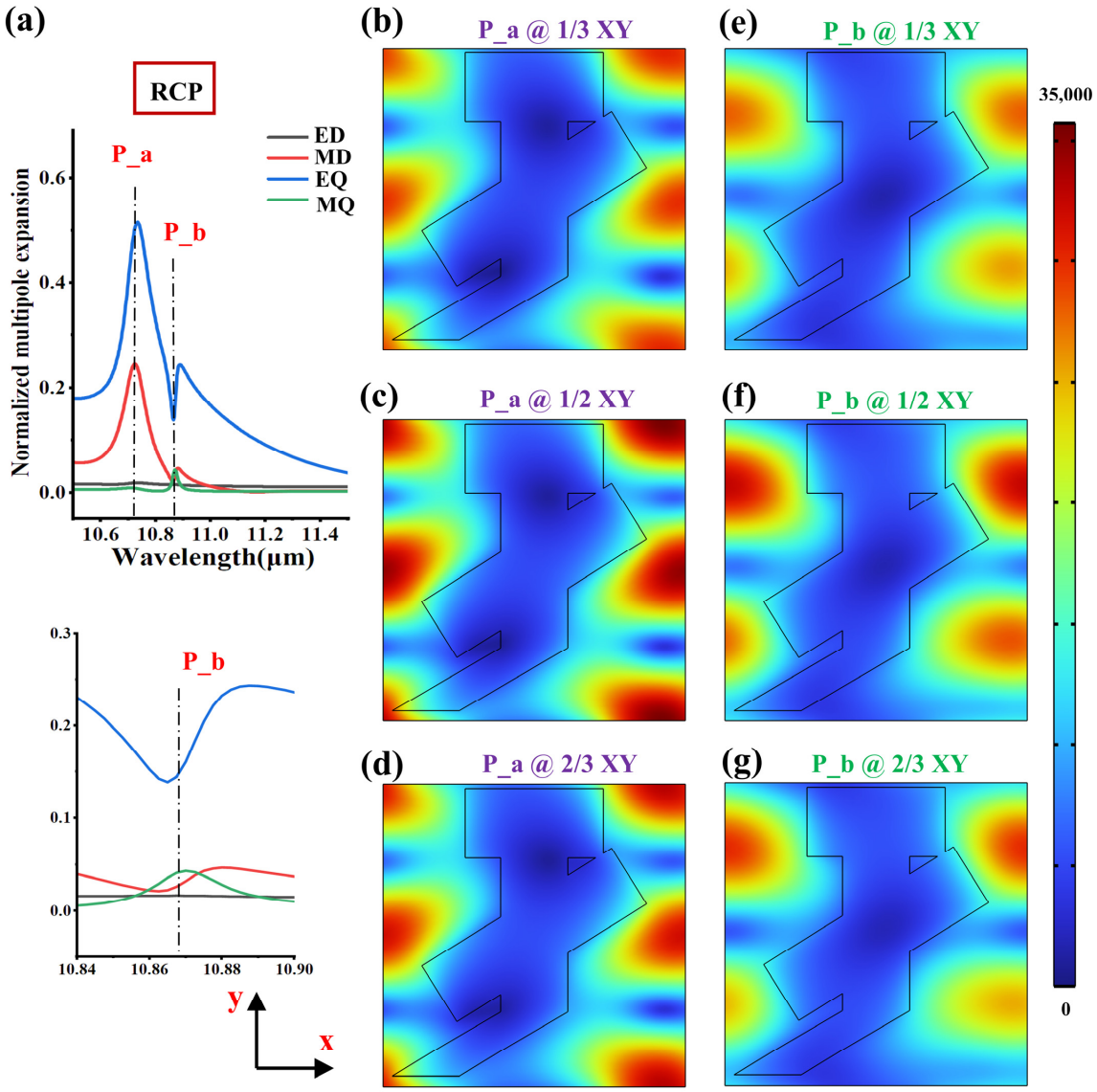


Figure 4. (**a**) Normalized multipole expansion spectra of the metasurface under RCP incidence. (**b**–**d**) XY cross-sectional view of the metasurface's magnetic field intensity at peak *a*. (**e**–**g**) XY cross-sectional view of the metasurface's magnetic field intensity at peak *b*. "1/3", "1/2" and "2/3" respectively indicate that the cross-sections are located at 1/3, 1/2 and 2/3 of the thickness of the metasurface.

In addition, Figure 5a shows the multipole expansion spectrum of the oracle bone inscriptions metasurface under LCP incidence. At the wavelength corresponding to valley a, the transmission minimum arises from the coupled contributions of MQ, EQ, and MD. Figure 5b–d show the magnetic-field-intensity distributions of the metasurface at valley a. A clear standing-wave localization can still be observed along the x-direction, and its intensity is noticeably stronger than that under RCP incidence in Figure 4, suggesting that this resonance is responsible for the transmission dip. In contrast, the standing-wave density along the y-direction is lower than that in Figure 4b–g, indicating that the equivalent wave vector ky at valley a is weaker than those at peaks a and b. These differences in resonant field distribution under opposite helicities provide further evidence for the multi-wavelength circular dichroism of the proposed metasurface.

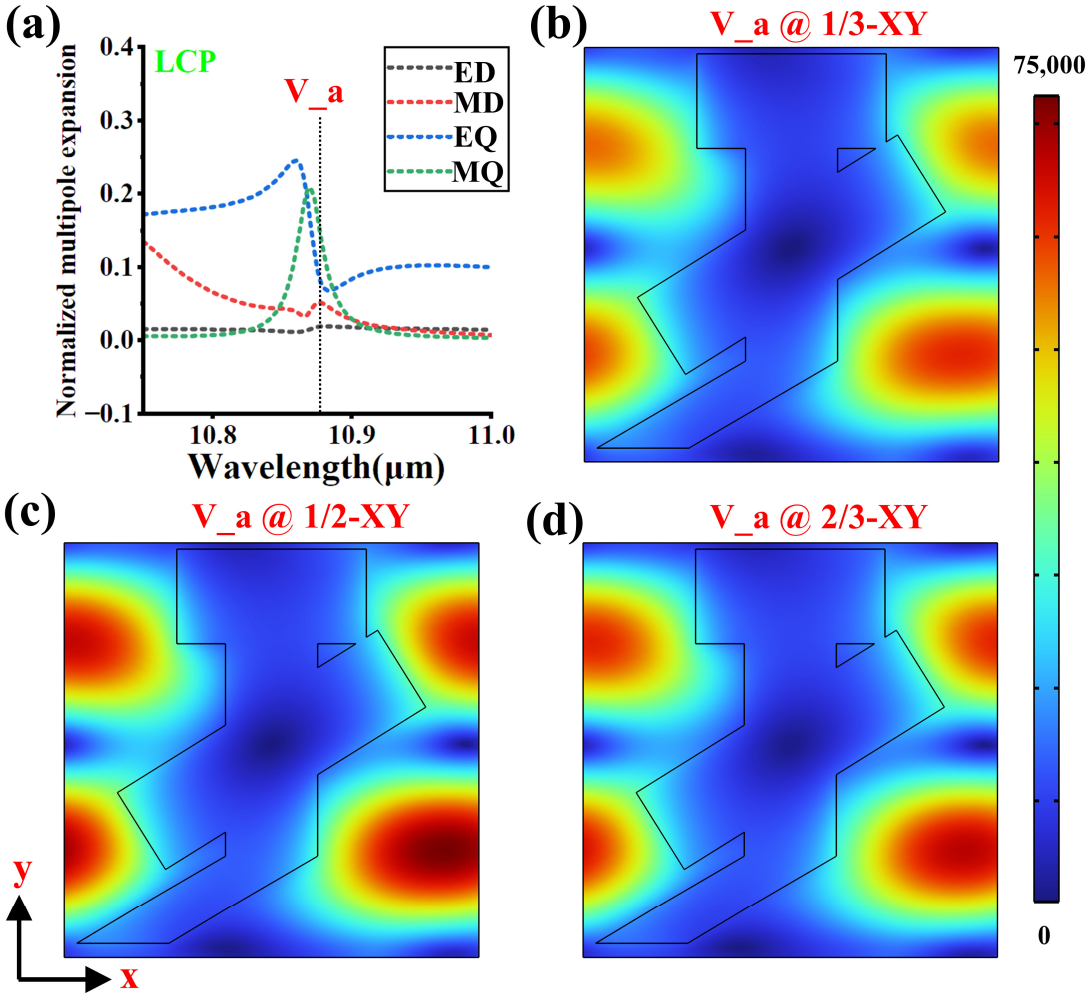


Figure 5. (**a**) Normalized multipole expansion spectrum of the metasurface under LCP incidence. (**b**–**d**) XY cross-sectional view of the magnetic field intensity of the metasurface at the wavelength of valley *a*.

3.3. Potential Error Analysis

In the previous sections, we analyzed the full evolution of the chiral structure of the oracle-bone-inspired metasurface and examined the physical origin of the target resonant peaks, which were ultimately attributed to the coupling of multiple resonators. In this subsection, we further assess how key fabrication and simulation parameters influence the optical response in order to evaluate both fabrication tolerance and numerical reliability. As shown in Figure 6a, under-etching, namely an insufficient etching depth that leaves a

residual silicon layer, significantly weakens the CD response. When the thickness of the residual silicon film exceeds 80 nm, the CD value already shows obvious degradation. By contrast, over-etching, where the etch penetrates through the silicon layer and extends into the MgF_2 substrate, has a much weaker effect on device performance. Even when the over-etching depth reaches 300 nm, the CD response is still maintained, as shown in Figure 6b. The numerical results also remain stable with respect to the simulation settings. As shown in Figure 6c, the CD spectrum changes very little when the mesh size varies from 20 nm to 100 nm, indicating that the calculated results are not sensitive to the discretization conditions. In addition, Figure 6d shows that when the thickness of the PML exceeds 4000 nm, the outwardly scattered light can be fully absorbed, thereby ensuring the convergence of the simulation. These results confirm that the proposed structure is reasonably tolerant to fabrication deviations and that the simulation parameters used here are sufficient to produce reliable results. More details of the error analysis can be found in the Supplementary Materials.

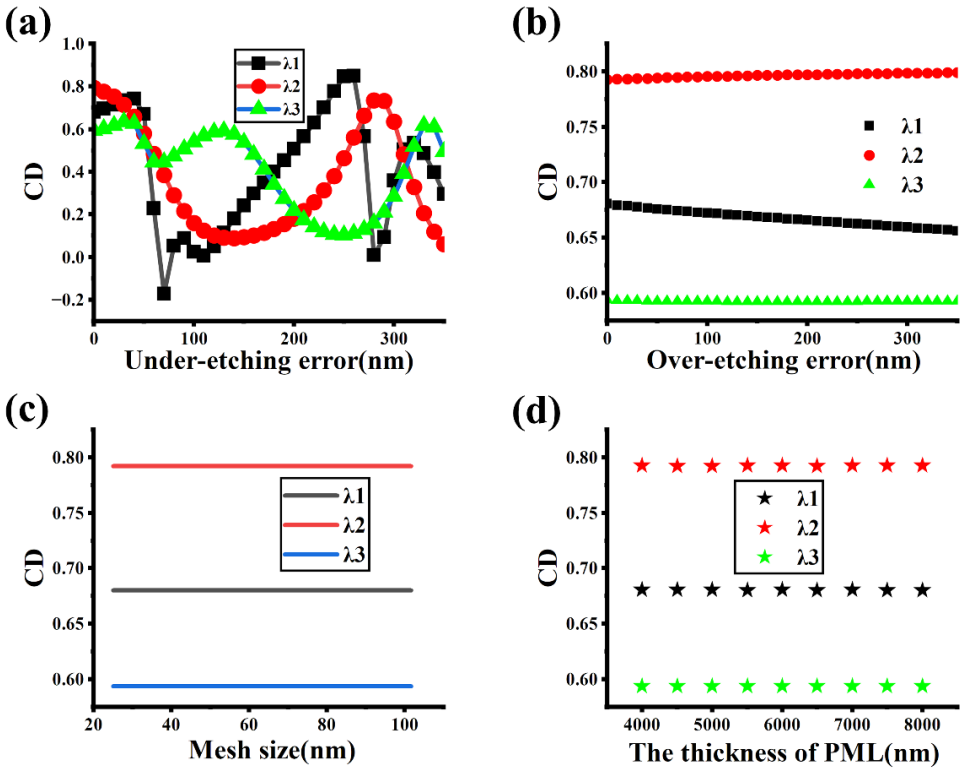


Figure 6. (**a**) The influence of under-etching depth error on the optical model. (**b**) The influence of over-etching depth error on the optical model. (**c**) The influence of the mesh size on the optical model. (**d**) The influence of the PML thickness on the optical model.

4. Discussion and Conclusions

Although the proposed single-layer metasurface exhibits three pronounced CD peaks in the long-wave infrared region, several issues still need to be addressed for practical applications. The current peak spacings (~0.4 μm and ~0.1 μm) are too narrow for independent channel imaging in focal-plane arrays. Future studies should therefore optimize the peak spacing by tuning the dislocation, lattice period, and refractive index so that the spectral positions better match standard LWIR imaging arrays [32,33]. Another important direction is monolithic integration with LWIR detectors [34,35], such as InAsSb devices, to realize compact pixels for CD sensing. Beyond imaging, the platform holds promise for vibrational circular dichroism (VCD) sensing and polarization multiplexing. For VCD applications [36–38], a thin chiral molecular layer could be deposited onto the metasur-

face, and the difference in transmission between LCP and RCP could then be measured to evaluate multi-wavelength enhancement. For polarization multiplexing [39,40], three independent channels may be implemented by modulating the circular polarization state at each resonance. The dislocation–rotation design strategy is not limited to a specific material system or spectral band. In addition, by adjusting the lattice constants and dislocation, the geometry can be transferred to the visible, near-infrared, or terahertz bands, enabling custom multi-wavelength chiral devices for 3D displays, quantum communication, and non-destructive testing.

In summary, we have designed and verified a novel chiral metasurface inspired by the structure of oracle bone script. By combining dislocation with rotational symmetry breaking in a single-layer planar architecture, the design achieves strong circular dichroism at three discrete wavelengths, with a maximum CD value of 0.79. This work addresses a key limitation of most existing high-performance chiral metasurfaces, which are typically restricted to a single operating wavelength. The proposed architecture combines clear physical design logic, structural simplicity, and practical scalability, thereby providing a promising platform for the development of multifunctional and customizable multi-wavelength chiral photonic devices. More broadly, this study expands the design strategy for chiral light manipulation and offers a useful basis for future work on integrated polarization optics, advanced biosensing, and spectral analysis.

Supplementary Materials: The following supporting information can be downloaded at: https://www.mdpi.com/article/10.3390/photonics13050491/s1. Figure S1. Band diagram of the photonic crystal corresponding to the metasurface. The vector on the horizontal axis is the wave vector in the x direction, ranging from the Γ point to the X point. The solid lines represent the eigenmodes corresponding to the metasurface, and the dashed lines represent the FP resonance modes. Table S1: Comparison of the performance with recently published chiral metasurfaces [25,41–45].

Author Contributions: Conceptualization, B.C. and T.X.; methodology, B.C. and Y.Z.; software, L.L. and T.X.; validation, G.S., T.X. and Y.Z.; formal analysis, B.C. and T.X.; investigation, Y.Z. and G.S.; resources, L.L.; data curation, T.X.; writing—original draft preparation, B.C. and T.X.; writing—review and editing, K.Z. and H.S.; visualization, K.Z.; supervision, H.S.; project administration, H.S.; funding acquisition, K.Z. and H.S. All authors have read and agreed to the published version of the manuscript.

Funding: This research was funded by the National Key Research and Development Program of China, grant number NO. 2024YFB2807803; This research was funded by the Natural Science Foundation of Tianjin, grant number NO. 24JCQNJC01880; This research was funded by the Young Elite Scientists Sponsorship Program of Cast, grant number NO. YESS20240775; This research was funded by the Strategic Priority Research Program of the Chinese Academy of Sciences (grant no. XDB0980000).

Institutional Review Board Statement: Not applicable.

Informed Consent Statement: Not applicable.

Data Availability Statement: The raw data supporting the conclusions of this article will be made available by the authors on request.

Conflicts of Interest: The authors declare no conflicts of interest.

References

1. Bhupathi, P.; Hwang, J.; Martin, R.M.; Blankstein, J.; Jaworski, L.; Mulders, N.; Tanner, D.B.; Lee, Y. Aerogel waveplates. *Opt. Express* **2009**, *17*, 10599–10605. [CrossRef] [PubMed]
2. Aiello, A.; Marquardt, C.; Leuchs, G. Nonparaxial polarizers. *Opt. Lett.* **2009**, *34*, 3160–3162. [CrossRef] [PubMed]
3. Gagnon, Y.L.; Templin, R.M.; How, M.J.; Marshall, N.J. Circularly Polarized Light as a Communication Signal in Mantis Shrimps. *Curr. Biol. CB* **2015**, *25*, 3074–3078. [CrossRef]

4. Walworth, V.K. Light polarization in support of stereoscopic display. *Opt. Eng.* **2012**, *51*, 1104. [CrossRef]
5. de Jong, J.J.D.; Lucas, L.N.; Kellogg, R.M.; van Esch, J.H.; Feringa, B.L. Reversible Optical Transcription of Supramolecular Chirality into Molecular Chirality. *Science* **2004**, *304*, 278–281. [CrossRef]
6. Cardano, F.; Marrucci, L. Spin–orbit photonics. *Nat. Photonics* **2015**, *9*, 776–778. [CrossRef]
7. Kwon, H.; Faraon, A. NEMS-Tunable Dielectric Chiral Metasurfaces. *ACS Photonics* **2021**, *8*, 2980–2986. [CrossRef]
8. Shi, T.; Deng, Z.-L.; Geng, G.; Zeng, X.; Zeng, Y.; Hu, G.; Overvig, A.; Li, J.; Qiu, C.-W.; Alù, A.; et al. Planar chiral metasurfaces with maximal and tunable chiroptical response driven by bound states in the continuum. *Nat. Commun.* **2022**, *13*, 4111. [CrossRef]
9. Won, R. Chiral spectrometer. *Nat. Photonics* **2017**, *11*, 208. [CrossRef]
10. Kuznetsov, A.I.; Brongersma, M.L.; Yao, J.; Chen, M.K.; Levy, U.; Tsai, D.P.; Zheludev, N.I.; Faraon, A.; Arbabi, A.; Yu, N. Roadmap for Optical Metasurfaces. *ACS Photonics* **2024**, *11*, 50. [CrossRef] [PubMed]
11. Doshi, S.; Ji, A.; Mahdi, A.I.; Keene, S.T.; Selvin, S.P.; Lalanne, P.; Appel, E.A.; Melosh, N.A.; Brongersma, M.L. Electrochemically mutable soft metasurfaces. *Nat. Mater.* **2025**, *24*, 205–211. [CrossRef]
12. Deng, Y.; Meng, C.; Thrane, P.C.V.; Sande, S.I.; Bozhevolnyi, S.I.; Ding, F. MEMS-integrated metasurfaces for dynamic linear polarizers. *Optica* **2024**, *11*, 326–332. [CrossRef]
13. Zhang, X.; Cui, X.; Cai, T.; Cai, W.; Low, T.; Chen, H.; Lin, X. Scattering-free Plasmonic Brewster Effect via Metasurfaces. *ACS Photonics* **2025**, *12*, 1865–1872. [CrossRef]
14. Zang, G.; Liu, Z.; Feng, S.; Zhu, W. A Polarization-Insensitive and Adaptively-Blazed Meta-Grating Based on Dispersive Metasurfaces. *Laser Photonics Rev.* **2025**, *19*, 2401031. [CrossRef]
15. Zheng, T.; Gu, Y.; Kwon, H.; Roberts, G.; Faraon, A. Dynamic light manipulation via silicon-organic slot metasurfaces. *Nat. Commun.* **2024**, *15*, 1557. [CrossRef] [PubMed]
16. Xia, Z.S.; Liu, Y.H.; Bao, Z.; Wang, L.H.; Wu, B.; Wang, G.; Wang, H.; Ren, X.G.; Huang, Z.X. Strong circular dichroism chiral metasurfaces generated by quasi bound state in continuum domain. *Acta Phys. Sin.* **2024**, *73*, 178102. [CrossRef]
17. Wang, C.; Wu, J.; Tian, J. High-Q Chiral Janus Metasurfaces Based on Multipolar Resonances. *Laser Photonics Rev.* **2025**, *19*, e00205. [CrossRef]
18. Wu, J.; Ouyang, C.; Ma, J.; Li, H.; Xu, Z.H.; Hao, X.; Xu, Q.; Gu, J.; Xu, S.; Li, Y. Reconfigurable BIC-Based Intrinsic Chiral All-Dielectric Terahertz Metasurfaces. *Laser Photonics Rev.* **2025**, *19*, e00674. [CrossRef]
19. Spinnler, B. Recent advances on polarization multiplexing. In *Proceedings of the 2008 Digest of the IEEE/LEOS Summer Topical Meetings*; IEEE: New York, NY, USA, 2008; pp. 227–228.
20. Yu, Y.; Yang, G.; Zhang, S.; Liu, M.; Xu, S.; Wang, C.; Li, M.; Zhang, X.A. Wide-Range and Highly Sensitive Chiral Sensing by Discrete 2D Chirality Transfer on Confined Surfaces of Au(I)-Thiolate Nanosheets. *ACS Nano* **2022**, *16*, 148–159. [CrossRef]
21. Deng, H.; Jiang, X.; Zhang, Y.; Zeng, Y.; Barkaoui, H.; Xiao, S.; Yu, S.; Kivshar, Y.; Song, Q. Chiral lasing enabled by strong coupling. *Sci. Adv.* **2025**, *11*, eads9562. [CrossRef]
22. Lin, D.; Ghaffari, A.; Gu, Q. Chiral Metasurfaces with Multidimensional Tunability for Optical Chiral States. *Adv. Opt. Mater.* **2025**, *13*, e01859. [CrossRef]
23. Cai, C.; Li, Y.; Zhou, Y.; Pan, Q. Chiral metasurfaces enabling tunable spin selection for multidimensional images and beam splitting. *Front. Phys.* **2025**, *20*, 064203. [CrossRef]
24. Overvig, A.; Yu, N.; Alù, A. Chiral Quasi-Bound States in the Continuum. *Phys. Rev. Lett.* **2021**, *126*, 073001. [CrossRef]
25. Cen, M.; Wang, J.; Cheng, M.; Lei, Z.; Li, Y.; Wang, Z.; Zhao, X.; Wu, Z.; Zhang, H.; Liu, Y.J. Moiré metasurfaces with tunable near-infrared-I chiroptical responses for biomolecular chirality discrimination. *Nanoscale* **2025**, *17*, 1970–1979. [CrossRef]
26. Liu, Q.-S.; Chao, M.-H.; Zhang, W.-J.; Song, G.-F. Dual-Band Chiral Nonlinear Metasurface Supported by Quasibound States in the Continuum. *Ann. Phys.* **2022**, *534*, 2200263. [CrossRef]
27. Ma, W.; Cheng, F.; Liu, Y. Deep-Learning-Enabled On-Demand Design of Chiral Metamaterials. *ACS Nano* **2018**, *12*, 6326–6334. [CrossRef]
28. Shkondin, E.; Takayama, O.; Panah, M.E.A.; Liu, P.; Lavrinenko, A.V. Large-scale high aspect ratio Al-doped ZnO nanopillars arrays as anisotropic metamaterials. *Opt. Mater. Express* **2017**, *7*, 1606–1627. [CrossRef]
29. Franta, D.; Neas, D.; Giglia, A.; Franta, P.; Ohlídal, I. Universal dispersion model for characterization of optical thin films over wide spectral range: Application to magnesium fluoride. *Appl. Surf. Sci.* **2017**, *421*, 424–429. [CrossRef]
30. Evlyukhin, A.B.; Fischer, T.; Reinhardt, C.; Chichkov, B.N. Optical theorem and multipole scattering of light by arbitrarily shaped nanoparticles. *Phys. Rev. B* **2016**, *94*, 205434. [CrossRef]
31. Alaee, R.; Rockstuhl, C.; Fernandez-Corbaton, I. An electromagnetic multipole expansion beyond the long-wavelength approximation. *Opt. Commun.* **2017**, *407*, 17–21. [CrossRef]
32. Zhu, T.; Wang, L.; Jing, W.; Deng, J.; Ye, J.; Zhang, Y.; Chu, Z.; Zhou, J.; Chen, X.; Li, X. Circular Polarimetric Imaging with a Metamaterial Integrated Long-Wavelength Infrared Focal Plane Array. *Adv. Sci.* **2025**, *39*, e09292. [CrossRef]
33. Wang, S.; Lu, L.; Zhu, L. Long-wave infrared computational multispectral metasurface and spectral reconstruction method. *Sci. Rep.* **2025**, *15*, 22274. [CrossRef]

34. Zhang, X.; Jiang, D.; Zhang, Y.; Zhao, Y.; Gao, F.; Li, C.; He, W.; Wang, D.; Hao, H.; Wu, D.; et al. Microhole array metasurface-enhanced InAs/GaSb superlattice LWIR detectors with boosted photoresponse via guided-mode resonance coupling. *Mater. Today* **2025**, *91*, 298–305. [CrossRef]
35. Wang, H.; Zou, Y.; Deng, G.; Song, L.; Gong, X.; Li, P.; Zhou, X.; Gao, X.; Ding, H.; Cheng, B.; et al. Design of multi-wavelength circularly polarized InAsSb photodetectors based on chiral silicon metasurfaces. *Appl. Opt.* **2026**, *65*, 2539–2546. [CrossRef]
36. Ye, L.; Li, J.; Richter, F.U.; Jahani, Y.; Lu, R.; Lee, B.R.; Tseng, M.L.; Altug, H. Dielectric Tetramer Nanoresonators Supporting Strong Superchiral Fields for Vibrational Circular Dichroism Spectroscopy. *ACS Photonics* **2023**, *10*, 4377–4384. [CrossRef]
37. Wei, Y.; Si, L.; Han, K.; Xu, H.; Bao, X.; Zhu, W. Quasi-BIC-enhanced integrated sensing dielectric metasurfaces for molecular fingerprint retrieval and chiral detection. *Nanoscale* **2025**, *17*, 8005–8015. [CrossRef]
38. Xu, C.; Ren, Z.; Zhou, H.; Zhou, J.; Ho, C.P.; Wang, N.; Lee, C. Metamaterial-Enhanced Vibrational Circular Dichroism for Mid-Infrared Spectroscopic Nanosensors. In Proceedings of the 2023 22nd International Conference on Solid-State Sensors, Actuators and Microsystems (Transducers), Kyoto, Japan, 25–29 June 2023; pp. 413–416.
39. Wang, J.; Chen, J.; Yu, F.; Wang, J.; Xing, H.; Chen, X.; Lu, W.; Li, G. Non-interleaved geometric phase metasurfaces for low-crosstalk circular polarization multiplexing. *Opt. Lett.* **2025**, *50*, 6630–6633. [CrossRef]
40. Song, S.; Liu, Q.; Luo, L.; Qi, L.; Yang, J.; Gong, Z.; Nandar Win, Z. Terahertz image encryption based on chiral metasurface. *Results Phys.* **2025**, *78*, 108485. [CrossRef]
41. Bai, J.; Wang, C.; Chen, X.; Basiri, A.; Wang, C.; Yao, Y. Chip-integrated plasmonic flat optics for mid-infrared full-Stokes polarization detection. *Photonics Res.* **2019**, *7*, 1051. [CrossRef]
42. Gao, Z.; Wang, P.; Xu, Z.; Zhao, T. Chiral metasurface absorber with near-infrared excitation-induced dual circular dichroism. *Opt. Laser Technol.* **2024**, *175*, 110826. [CrossRef]
43. Toftul, I.; Tonkaev, P.; Koshelev, K. Chiral Dichroism in Resonant Metasurfaces with Monoclinic Lattices. *PhysRevLett* **2024**, *133*, 216901. [CrossRef]
44. Cheng, B.; Zou, Y.; Song, G. Full-stokes polarization photodetector based on the chiral metasurface with the dislocated double gold rod configurations. *Opt. Laser Technol.* **2024**, *174*, 110531. [CrossRef]
45. Zhou, Y.; Huang, B.; Wang, Z.; Hong, W. Chiral metasurfaces with stabilized high circular dichroism empowered by BICs. *Opt. Commun.* **2024**, *568*, 130703. [CrossRef]

Disclaimer/Publisher's Note: The statements, opinions and data contained in all publications are solely those of the individual author(s) and contributor(s) and not of MDPI and/or the editor(s). MDPI and/or the editor(s) disclaim responsibility for any injury to people or property resulting from any ideas, methods, instructions or products referred to in the content.